The design and performance of the glass-scintillator hadronic calorimeter for the CEPC reference detector

Hua Cai,[1] Jinfan Chang,[2,3,4] Dejing Du,[2] Kun Ge,[5] Joao Guimaraes da Costa,[2,3,4] Fangyi Guo,[2,6] Jifeng Han,[7] Yuekun Heng,[2,3,4] Peng Hu,[8] Zhehao Hua,[2] Quan Ji,[2,3,4] Hengne Li,[9,*] Weichang Li,[10] Tao Lin,[2,3,4] Weiping Lin,[7] Jianbei Liu,[11] Xingquan Liu,[7] Yong Liu,[2,3,4] Guang Luo,[12] Yatian Pei,[2,3,4] Sen Qian,[2,3,4,†] Xusheng Qiao,[13] Jing Ren,[14] Manqi Ruan,[2,3,4] Bofeng Shang,[15] Weizheng Song,[2,3,4] Shengsen Sun,[2,3,4] Xinyuan Sun,[16] Gao Tang,[17] Xiyang Wang,[18] Xiaolong Wang,[18] Xin Wang,[2,3,4] Yifang Wang,[2,3,4] Shu Xian,[9] Yuguang Xie,[2,3,4] Dong Yang,[5] Haijun Yang,[19,‡] Boxiang Yu,[2,3,4] Rui Yuan,[19] Junsong Zhang,[2,3,4] Yang Zhang,[2,6] Yunlong Zhang,[11] Heng Zhao,[17] and Chunxiang Zhu[19]

[1]*China Building Materials Academy, Beijing 100024, China*
[2]*Institute of High Energy Physics, Chinese Academy of Sciences, Beijing 100049, China*
[3]*University of Chinese Academy of Sciences, Beijing 100049, China*
[4]*High Energy Physics Research Center, Henan Academy of Sciences, Zhengzhou 450046, China*
[5]*Beijing Glass Research Institute, Beijing 101111, China*
[6]*China Center of Advanced Science and Technology, Beijing 100190, China*
[7]*Key Laboratory of Radiation Physics and Technology of MOE, Sichuan University, Chengdu 610065, China*
[8]*China National Nuclear (Beijing) Nuclear Instrument Co., Ltd., Beijing 100176, China*
[9]*State Key Laboratory of Nuclear Physics and Technology, Institute of Quantum Matter, South China Normal University, Guangzhou 510006, China*
[10]*Shanghai Institute of Optics and Fine Mechanics, Chinese Academy of Sciences, Shanghai 201800, China*
[11]*Department of Modern Physics, University of Science and Technology of China, Hefei 230026, China*
[12]*School of Science, Sun Yat-sen University, No. 66 Gongchang Road, Shenzhen 518107, China*
[13]*State Key Laboratory of Silicon and Advanced Semiconductor Materials, Department of Materials Science and Engineering, Zhejiang University, Hangzhou 310027, China*
[14]*Key Laboratory of In-Fiber Integrated Optics of Ministry of Education, College of Physics and Optoelectronic Engineering, Harbin Engineering University, Harbin 150001, China*
[15]*School of Physics and Microelectronics, Zhengzhou University, Zhengzhou 450001, China*
[16]*Department of Physics, Key Laboratory of Jiangxi Province for Special Optoelectronic Artificial Crystal Materials, Jinggangshan University, Ji'an 343009, China*
[17]*College of Materials and Chemistry, China Jiliang University, Hangzhou 310018, China*
[18]*Fudan University, Shanghai 200433, China*
[19]*State Key Laboratory of Dark Matter Physics, Key Laboratory for Particle Astrophysics and Cosmology (MOE), Shanghai Key Laboratory for Particle Physics and Cosmology (SKLPPC), School of Physics and Astronomy & Tsung-Dao Lee Institute, Shanghai Jiao Tong University, Shanghai 200240, China*

The CEPC reference detector requires a particle-flow-oriented hadronic calorimeter with high three-dimensional granularity, sufficient depth, and robust neutral-hadron performance. Such a calorimeter is essential for the precision reconstruction of hadronic W, Z, and Higgs final states. The glass-scintillator hadronic calorimeter (GS-HCAL) is adopted as the baseline HCAL of the CEPC reference detector. It uses $40 \times 40 \times 10$ mm^3 gadolinium fluoro-oxide glass-scintillator cells read out by 3×3 mm^2 silicon photomultipliers, arranged in a barrel and two endcaps. The full detector comprises 5.22 million channels with a total depth of 6 λ_{I} and a sampling fraction of about 30%. Experimental studies of the baseline active unit show a light yield of ∼1500 ph/MeV and an attenuation length of about 6 cm. The glass scintillator retains more than 70% of its light yield after irradiation below 100 Gy, and practical single-cell signals have been measured with ^{137}Cs, cosmic-ray muon, and 5 GeV electron-beam sources. Geant4 simulation of the design predicts a standalone single-hadron energy resolution of $29.8\%/\sqrt{E} \oplus 6.5\%$ with non-linearity within 2%. Combined with particle-flow reconstruction, a boson mass resolution of 3.88% is achieved for the $H \to gg$ benchmark. Full prototype beam validation remains necessary to close the optical model, Birks quenching, intrinsic e/h, calibration, and system-level response. This study establishes the technical and performance basis of the GS-HCAL baseline design.

Keywords: glass scintillator; hadronic calorimeter; CEPC; silicon photomultiplier; particle-flow algorithm; highly granular calorimeter

I. INTRODUCTION

The Circular Electron–Positron Collider (CEPC) [1] is designed to measure Higgs boson couplings to sub-percent precision. It will also enable sensitive electroweak and flavour studies at centre-of-mass energies around the Z pole, the

* Corresponding author, Hengne.Li@m.scnu.edu.cn
† Corresponding author, qians@ihep.ac.cn
‡ Corresponding author, haijun.yang@sjtu.edu.cn

WW threshold, and the Higgs production peak [2]. Reconstructing the hadronic decays of W, Z, and Higgs bosons with the requisite resolution demands a calorimeter system that substantially exceeds conventional performance. The Particle-Flow Algorithm (PFA) [3, 4] achieves this by combining tracking and calorimeter information to reconstruct individual particles, separating charged- and neutral-hadron energy deposits on a cell-by-cell basis. This particle-level separation requires fine three-dimensional calorimeter granularity to resolve overlapping showers and assign each energy deposit to the correct parent particle.

Within a PFA-based detector, the hadronic calorimeter (HCAL) serves two defining roles. It provides the transverse and longitudinal segmentation needed for charged–neutral shower separation, and it supplies the intrinsic energy resolution for neutral hadrons, whose energies are inaccessible to the tracker. The CEPC Conceptual Design Report [1] specifies a boson mass resolution (BMR) of 3–4% for hadronic W, Z, and Higgs decays. Meeting this benchmark constrains the active medium to combine sufficient density for sampling performance, adequate light output for efficient readout, and manufacturability at the scale of millions of channels.

The glass-scintillator hadronic calorimeter (GS-HCAL) has been adopted as the HCAL of the CEPC reference detector [2]. It employs $40 \times 40 \times 10$ mm^3 cells of gadolinium fluoro-oxide (GFO) glass scintillator, each read out by a 3×3 mm^2 silicon photomultiplier (SiPM), arranged in 48 sampling layers within a barrel and two endcaps. The supporting evidence spans measured GFO material properties, single-cell signal verification, full-detector simulation projections consistent with the BMR target, and engineering feasibility studies at the CEPC detector scale.

This paper presents a coherent technical basis for the GS-HCAL. Section II derives the detector requirements from the physics goals and presents the architecture, active-medium selection, and readout technology. Section III reports the experimental characterisation of GFO glass and single-cell performance. Section IV describes the digitisation-based simulation framework and presents projected single-hadron and $H \to gg$ boson mass resolution. Section V discusses mechanical feasibility, calibration strategy, and the prototype validation programme, and Section VI summarises the findings.

The CEPC Reference TDR documents the entire reference detector, including all HCAL engineering, mechanical design, and alternative technology options, in exhaustive detail [2]. This paper is the first standalone, peer-reviewed account dedicated to the glass-scintillator HCAL (GS-HCAL). It presents a focused, physics-motivated synthesis that links GFO glass material properties, single-cell measurements, full-detector simulation, and the $H \to gg$ boson-mass-resolution benchmark into one coherent argument. Readers are referred to the TDR for the complete engineering, mechanical, and alternative-option detail not repeated here. [NEW-ANALYSES PLACEHOLDER: quantitative results added beyond the TDR, to be finalized]

II. DETECTOR DESIGN

A. Design requirements

The boson mass resolution target of 3–4% established in Section I defines the performance scale that the HCAL must achieve. The PFA reconstruction paradigm governs how this performance is realised. Within the PFA approach, charged-hadron momenta are measured by the central tracker. The HCAL therefore contributes primarily shower-shape and cluster-position information for pattern recognition. For neutral hadrons, which leave no track, the HCAL alone determines both energy and position. The HCAL must therefore provide fine three-dimensional granularity—both transverse and longitudinal—to separate nearby charged and neutral showers. It must also provide adequate intrinsic energy resolution for neutral hadrons. These dual requirements translate into three design drivers. First, the granularity must be sufficient to resolve individual shower clusters in the dense environment of a hadronic jet. Second, the longitudinal depth must be sufficient to contain the full development of hadronic showers. Third, the sampling fraction must be high enough to keep the stochastic term of the energy resolution within the required bounds.

Meeting these requirements at the CEPC detector scale involves coupled trade-offs that must be resolved at the level of the active medium, cell geometry, and readout architecture. Increasing the density of the active medium improves the sampling fraction and hence the stochastic resolution. This is beneficial only if optical transmission and light yield remain adequate to produce a usable signal at the SiPM. Reducing the cell size improves shower-separation capability for PFA, but increases the number of readout channels and with it the complexity and cost of electronics, cooling, and calibration. A shorter attenuation length can be tolerated in small cells, where the optical path lengths are correspondingly short, but this same attenuation length would become prohibitive in larger cells. The design choices described in the following subsections represent the resolution of these trade-offs, informed by measured material properties, simulation studies, and engineering feasibility assessments.

B. Detector architecture

The GS-HCAL is a steel-scintillator sampling calorimeter comprising 48 longitudinal layers arranged in a barrel and two endcaps. It reaches a total depth of $6\,\lambda_{\mathrm{I}}$ and contains 5.22 million (5,224,960 in total) readout channels. The barrel is divided into 16 trapezoidal sectors forming a hexadecagonal prism that approximates a cylindrical shell. It has an inner radius of 2140 mm, an outer radius of 3455 mm, a length of 6460 mm, and a mass of about 955 t. The two endcaps use matching 16-sector disk structures with inner and outer radii of 400 mm and 3385 mm, extending in $|z|$ from 3260 mm to 4575 mm, each weighing about 362 t. The sectorisation supports modular assembly. Glass scintillator (GS) cells, SiPMs, printed circuit boards (PCBs), and application-specific inte-

grated circuits (ASICs) are assembled into boxes that can be tested before installation. Water-cooling pipes are embedded in the steel absorber layers, with a design target of 15 mW per front-end channel. The overall geometry is shown in Fig. 1, and Table 1 summarises the cell, box, layer, and sector counts for the barrel and endcaps.

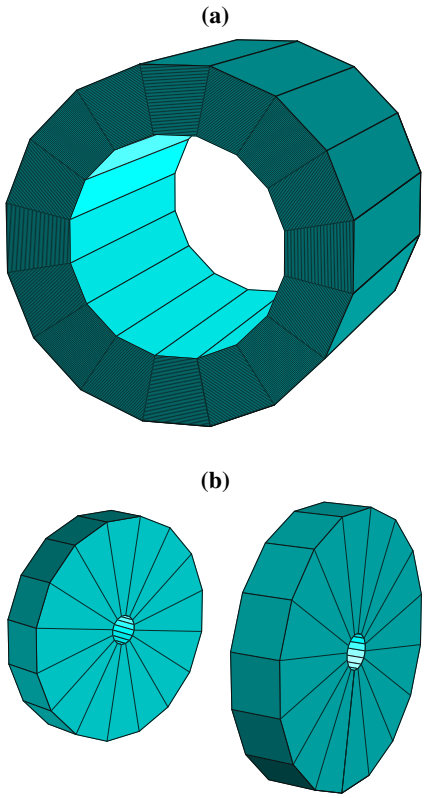

Fig. 1: (a) Barrel: 16 trapezoidal sectors forming a cylindrical structure. (b) Endcap: disk with matching sector segmentation.

TABLE 1: Numbers of cells, boxes, layers, and sectors for the barrel and endcaps in the GS-HCAL.

Part	Cells	Boxes	Layers	Sectors
Barrel	3 212 800	27 840	48	16
Endcap ($\times 2$)	1 006 080	3072	48	16

The single-layer design is the fundamental repeating unit of the design detector, and the same layer structure is used throughout the barrel and endcaps to simplify calibration and digitisation modelling. Each layer has a total thickness of 27.0 mm and comprises a 9.8 mm steel absorber, a 10 mm GS active layer, a 3.2 mm PCB/ASIC layer, and two 2 mm steel cover plates. The nuclear-interaction-length contributions of the steel absorber, GS, and PCB are $0.0805\,\lambda_{\mathrm{I}}$, $0.0425\,\lambda_{\mathrm{I}}$, and $0.0024\,\lambda_{\mathrm{I}}$, respectively, giving a ratio of about $1 : 0.53 : 0.03$. The sampling fraction, defined as the fraction of dE/dx deposited in the active GS layer for minimum-ionising particles (MIPs), is about 30% [2]. This energy-sampling fraction in the active medium is conceptually distinct from the nuclear-interaction-length fractions listed above. Those fractions describe the geometric probability of hadronic interactions occurring in each sub-layer. The single-layer structure and cell geometry are illustrated in Fig. 2.

The 48-layer segmentation is motivated by the need for adequate longitudinal shower sampling. With a total depth of $6\,\lambda_{\mathrm{I}}$, the GS-HCAL provides sufficient hadron containment while keeping the detector volume within the magnet cryostat envelope. Each of the 48 longitudinal samples corresponds to $0.125\,\lambda_{\mathrm{I}}$, affording detailed shower-profile reconstruction along the depth axis. The upstream electromagnetic calorimeter (ECAL) contributes about $1.2\,\lambda_{\mathrm{I}}$ of additional material, so the total interaction length before the magnet coil exceeds $7\,\lambda_{\mathrm{I}}$.

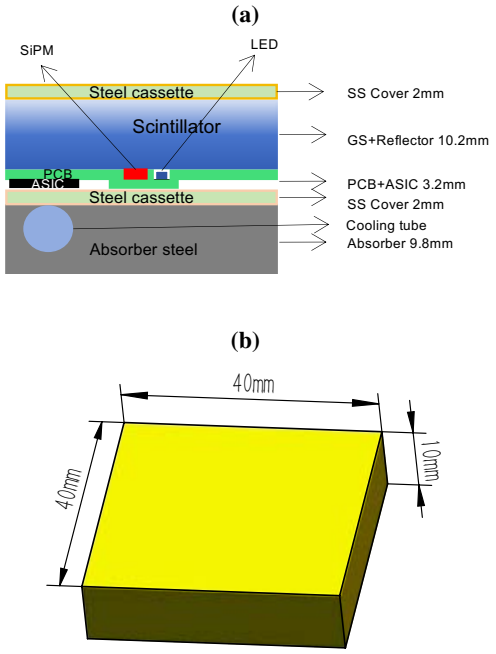

Fig. 2: (a) Single-layer structure of the GS-HCAL, showing the steel absorber, GS active layer, PCB/ASIC layer, cover plates, and embedded cooling pipes. (b) One $40 \times 40 \times 10$ mm^3 GS cell.

C. Active medium and readout

The detector architecture described above imposes specific requirements on the active medium, photosensor, and readout electronics. Each technology choice is driven by a causal chain that connects back to the physics requirements.

Active medium. GFO glass is adopted as the active medium because it provides a practical balance of density, light output, and manufacturability for highly granular calorimetry. The choice is motivated by the density–light-yield trade-off identified in Section II A. A high-density active medium is needed to raise the sampling fraction and

thereby improve the stochastic resolution. However, the density must not come at the cost of optical opacity or unacceptably low light yield. GFO glass has a density of 6.0 g/cm^3. This value is substantially higher than conventional plastic scintillator (typically $\sim$1.05 g/cm^3) and approaches that of crystalline BGO (7.13 g/cm^3). It has a nuclear interaction length of 24.2 cm and a dE/dx of 8.0 MeV/cm for MIPs. This high density yields a sampling fraction of about 30%. This is roughly twice the value expected for a plastic-scintillator AHCAL with the same absorber geometry. The higher sampling fraction is expected to reduce the stochastic term of the energy resolution. A direct simulation comparison with a plastic-scintillator design of identical absorber layout has not yet been performed. At the same time, the measured light yield of $\sim$1500 ph/MeV is sufficient for cell-level calorimetry when read out by a SiPM. The value of 1000 ph/MeV is adopted as the tile production quality threshold. The emission peak near 400 nm matches the peak PDE of commercial SiPM devices. The GFO material builds on earlier glass-scintillator development [5] and recent progress in Ce-doped heavy glass compositions [6–8]. Table 2 compares key GFO parameters with BGO crystal [9] and DSB glass [10]. This comparison shows that GFO occupies a distinct region of the parameter space. It has higher density than DSB. It offers lower cost and better mouldability than BGO. Its light yield is adequate for SiPM readout in $40 \times 40 \times 10$ mm^3 cells.

TABLE 2: Key parameters of GFO glass compared with BGO [9] and DSB [10]. GFO parameters are from Refs. [6–8], measured on a $5 \times 5 \times 5$ mm^3 sample.

Parameter	GFO	BGO	DSB
Density (g/cm^3)	6.0	7.13	4.2
Melting point ($^\circ$C)	1250	1050	1550
Radiation length (cm)	1.59	1.12	2.62
Molière radius (cm)	2.49	2.23	3.33
Nuclear interaction length (cm)	24.2	22.7	31.8
Z_{eff}	56.6	71.5	49.7
dE/dx (MeV/cm)	8.0	8.99	5.9
Emission peak (nm)	400	480	430
Refractive index	1.74	2.15	—
Light yield (ph/MeV)	$\sim$1500	7500	2500
Energy resolution (% at 662 keV)	$\sim$23	9.5	—
Scintillation decay time (ns)	$\sim$60, 500	60, 300	90, 400

Cell geometry. The choice of $40 \times 40 \times 10$ mm^3 cells follows directly from the PFA requirement for fine transverse granularity. Hadronic showers in a dense calorimeter extend laterally over several centimetres. Cell dimensions significantly smaller than the typical lateral shower extent are needed to resolve individual shower cores and to separate the charged and neutral components within a jet. The 40 mm transverse pitch is comparable to that of other highly granular HCAL designs and has been shown to provide adequate pattern recognition in PFA studies [3, 11]. At the same time, 40 mm is small enough that optical path lengths within the tile are short. The measured attenuation length of about 6 cm at 400 nm is therefore acceptable. The maximum path length from the far corner of a 40×40 mm^2 tile to a centrally placed SiPM is of order 30 mm, well within the attenuation range. If larger cells were used, the attenuation length would become a limiting factor for response uniformity. If cells were smaller, the channel count would increase rapidly, with attendant cost and power implications for the readout system. The 10 mm cell thickness corresponds to the active depth per sampling layer and is chosen to balance the active-to-passive ratio against the longitudinal sampling frequency.

SiPM readout. Silicon photomultipliers are adopted as the photosensor. They combine compact dimensions (3×3 mm^2 active area), insensitivity to magnetic fields, high photon detection efficiency (PDE) near 400 nm, and single-photon sensitivity. These features are essential for reading out small GFO tiles in the 3.5 T CEPC solenoid field. The three key requirements for the SiPM are adequate PDE at the GFO emission wavelength, sufficiently low dark-count rate (DCR), and mechanical dimensions compatible with 40 mm cell pitch. The low DCR must permit a low readout threshold. Table 3 lists representative commercial devices. The Hamamatsu Photonics (HPK) S14160-3050 and Novel Device Laboratory (NDL) EQR20-11-3030 are the most promising candidates.

The HPK S14160-3050 provides a PDE of 47% at 400 nm and a DCR in the range 10–100 kHz/mm^2. The NDL EQR20-11-3030 provides 45% PDE at 400 nm with a DCR of 150–450 kHz/mm^2. The cell light output of about 60 photoelectrons per MIP (p.e./MIP), together with these SiPM parameters, supports a 0.1 MIP readout threshold (about 5–6 p.e.). At this threshold the measured noise-occupancy rates are 12 Hz/mm^2 for the HPK device and 28 Hz/mm^2 for the NDL device. These rates include correlated noise from afterpulsing and optical crosstalk and are derived from the single-photoelectron DCR values and the SiPM pulse-height distribution. The 0.1 MIP threshold is chosen because it provides adequate signal-to-noise margin while keeping the noise occupancy comfortably below values that would degrade cluster reconstruction. These noise-occupancy figures correspond to un-irradiated devices. The effect of CEPC radiation doses (40–96 Gy) on SiPM dark-count rate has not been directly measured in this study. However, the baseline noise occupancy at the 0.1 MIP threshold is sufficiently low that a moderate radiation-induced increase would remain acceptable for cluster reconstruction. Dedicated irradiation tests of candidate SiPMs to CEPC-representative doses are planned as part of the prototype programme. The three-pixel-pitch comparison in Table 3 also illustrates the trade-off between PDE and dynamic range. The 15 µm pitch HPK S14160-3015PS offers a higher pixel count and larger effective dynamic range but lower PDE (27% at 400 nm). This makes it less suitable for the low-light regime of GFO scintillation. The 50 µm pitch devices (HPK S14160-3050HS, NDL EQR20-11-3030, Jiabei Technology (JBT) JSP-TP3050-SMT) provide higher PDE at the cost of fewer pixels and a correspondingly smaller linear dynamic range. This trade-off is acceptable given the moderate light output of GFO tiles.

Front-end electronics. The front-end readout must preserve single-cell signal information while scaling to 5.22

TABLE 3: Parameters of commercial SiPMs evaluated for the GS-HCAL.

Parameter	HPK		NDL	JBT
Type	S14160-3015PS	S14160-3050HS	EQR20-11-3030-S	JSP-TP3050-SMT
Pixel pitch (µm)	15	50	20	50
Number of pixels	39 984	3531	22 500	3364
Terminal capacitance (pF)	530	500	157.5	170
Breakdown voltage (V)	38 ± 3	38 ± 3	27.2 ± 1	24.6 ± 0.2
Recommended V_{op} (V)	$V_{\mathrm{BD}} + 3$	$V_{\mathrm{BD}} + 2.7$	$V_{\mathrm{BD}} + 5$	$V_{\mathrm{BD}} + 2$
Peak-sensitivity wavelength (nm)	450	450	420	420
Peak PDE (%)	32	50	47.8	35
PDE at 400 nm (%)	27	47	45	33
Gain	3.6×10^5	2.5×10^6	8.0×10^5	2.1×10^6
Total DCR at 1 p.e. (kHz/mm^2)	700 to 2100	10 to 100	150 to 450	120 to 270

million channels and operating within a tight power budget set by the water-cooling capacity. An interim front-end board [14] provides a gain of ± 20 V/V, bandwidth of 400 MHz, and baseline noise of $300\,\mu\mathrm{V_{RMS}}$. This board serves as the readout basis for the single-cell and prototype measurements and represents the performance envelope for a dedicated ASIC. The target ASIC specification includes a charge dynamic range of 0.8 pC–800 pC (corresponding to about 0.01–100 MIP), a charge resolution of 10% at 1 MIP, and a per-channel power consumption of 15 mW. The total ionising dose accumulated in the HCAL over the full 10-year Higgs programme is about 40 Gy. For one year of Z-pole operation the dose reaches about 96 Gy. The electronics are required to survive this radiation environment without significant performance degradation.

Optical simulation. Optical photon transport simulation with Geant4 [13] supports the interpretation of the design choices and provides parameter sensitivity studies. The simulation framework follows the methodology of Ref. [12], originally developed for aluminoborosilicate glass scintillator. Material-specific optical parameters (refractive index, attenuation length, scintillation yield, and surface reflectivity) are taken from the GFO measurements reported in Table 2 and in Section III. With these inputs the simulation predicts a response of about 42 p.e./MIP for the $40 \times 40 \times 10$ mm^3 cell with a centrally coupled 3×3 mm^2 SiPM and Teflon wrapping. This predicted value should be understood as conditional on the present modelling assumptions. The methodology was developed for a different glass composition. The substitution of GFO-specific optical parameters introduces systematic uncertainties that are yet to be fully quantified. A comparison of this optical-simulation prediction with measured cosmic-ray and beam-test responses is presented in Section III. There it is shown that the measurement exceeds the simulation by roughly 50%. This indicates that a GFO-specific optical-model tuning is required. The present simulation is retained for future parameter-sensitivity studies, while final validation of the optical model remains a prototype beam-test objective.

III. EXPERIMENTAL CHARACTERISATION

The technology choices described in Section II C are validated by experimental measurements of the GFO active medium and of complete single-cell assemblies. Two bodies of data are presented below. First, the bulk optical and radiation-tolerance properties of the glass itself define the parameter space available for cell design. Second, the photoelectron response of wrapped $40 \times 40 \times 10$ mm^3 cells under three complementary irradiation conditions establishes the practical signal level at the SiPM readout. Together these measurements connect the candidate material to a functioning active unit.

A. GFO material properties

The production-quality requirement for the active medium is a light yield of at least 1000 ph/MeV when read out with a photomultiplier tube (PMT) at the single-photoelectron level. GFO glass can achieve light yields well above 1000 ph/MeV. The best laboratory samples reach ∼1500 ph/MeV (Table 2). The visible transmittance exceeds 80% for polished samples of millimetre thickness. The emission spectrum peaks near 400 nm. The scintillation decay profile comprises a fast component of about 60 ns and a slower component of about 500 ns. These properties are sufficient for SiPM-coupled readout at the cell scale adopted here. The 400 nm emission peak coincides with the high-PDE region of commercial SiPMs (Table 3). The decay timing is compatible with the shaping and readout scheme of the nominal front-end electronics [14].

The optical attenuation length at the emission wavelength is obtained from transmittance measurements for varying thicknesses. The formula is $L_{\mathrm{att}} = (L_2 - L_1)/\ln(T_{L_1}/T_{L_2})$, where T_{L_1} and T_{L_2} are the measured transmittances at sample thicknesses L_1 and L_2, respectively [24]. The best GFO samples give $L_{\mathrm{att}} \approx 6$ cm at 400 nm (Fig. 3). For the $40 \times 40 \times 10$ mm^3 cell with a centrally coupled SiPM, the maximum photon path length is about 3 cm. The measured attenuation is acceptable for the present geometry. Improvement in attenuation length would nevertheless benefit position-dependent response uniformity. It remains a contin-

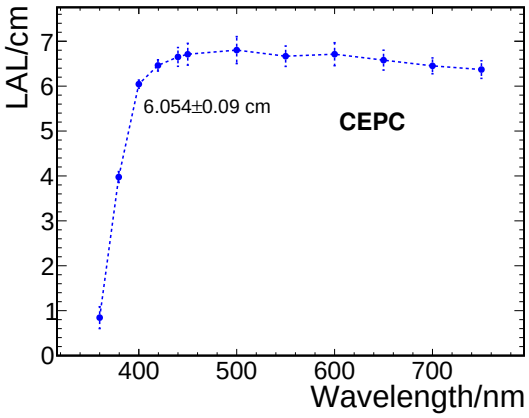

Fig. 3: Attenuation length of GFO glass as a function of wavelength, determined from transmittance measured at several sample thicknesses. At the emission peak (400 nm) the attenuation length is about 6 cm.

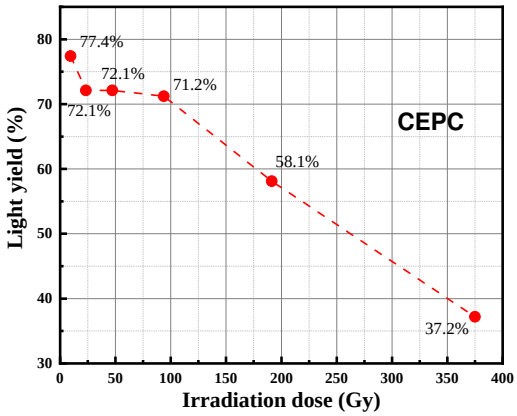

Fig. 4: Relative light yield of GFO glass as a function of gamma-irradiation dose. The retention is 71.2% at 100 Gy and 37.2% at 400 Gy. The CEPC ten-year Higgs dose (40 Gy) and one-year Z-pole dose (96 Gy) lie within the high-retention plateau.

uing goal of the material development programme [6–8].

Radiation tolerance is a practical requirement for the CEPC environment. The accumulated dose over the ten-year Higgs programme is estimated to be about 40 Gy. For one year of Z-pole operation the dose reaches about 96 Gy. These values are modest relative to hadron-collider environments but are nonetheless relevant for scintillator stability. Gamma-irradiation studies (Fig. 4) show that GFO glass retains 71.2% of its initial light yield at 100 Gy and 37.2% at 400 Gy [2, 19]. Proton-irradiation tests at the APEP facility [17] give consistent results [18], supporting the applicability of these retention values to the CEPC radiation environment. The CEPC operating range lies well within the high-retention plateau. The measured tolerance supports the intended use, provided that production batches are monitored and irradiation-induced response changes are tracked by the in-situ calibration system (Section V A).

B. Single-cell measurements

The effective light output of a $40 \times 40 \times 10$ mm^3 GFO cell coupled to a SiPM has been measured with three complementary probes. These are a ^{137}Cs radioactive source, cosmic-ray muons, and a 5 GeV electron beam at the KEK test-beam facility. In all three measurements the cell was wrapped in Teflon film [16] and the SiPM was positioned at the centre of one $40 \times 40 \times 10$ mm^3 face. Teflon was selected after comparative measurements showed about 20% higher effective reflectivity than Enhanced Specular Reflector (ESR) film (3M) [16] for the present cell geometry. The SiPM models differ among the three measurements because the data were collected at different times as device availability evolved. All three devices are representative of the reference specifications listed in Table 3. The results are normalised to photoelectrons (p.e.), the physically meaningful quantity for comparing across different SiPM types.

The ^{137}Cs measurement used an HPK S14160-3050HS SiPM. The 662 keV γ-ray pulse-height spectrum yields a most probable value (MPV) of 12.9 p.e. at the Compton edge, as shown in Fig. 5(a). This result characterises the response to a point-like γ-ray conversion within the cell volume. Because the energy deposition geometry differs fundamentally from that of a through-going MIP, the ^{137}Cs signal is not directly scalable to a MIP-equivalent value. It provides an independent verification of the single-cell signal chain and an estimate of the average photon-collection efficiency.

The fiducial MIP-scale reference is provided by cosmic-ray muons, which are genuine MIPs that traverse the full 10 mm cell thickness and deposit energy at a well-understood rate. The measurement employed an HPK S13360-3050PE SiPM and gave 63.6 ± 0.5 p.e./MIP. Here, 1 MIP corresponds to the most probable energy deposit of a minimum-ionising muon in the GFO cell (Fig. 5(b)). The quoted ± 0.5 p.e./MIP is the statistical fit uncertainty only. Dominant systematic uncertainties arise from the SiPM PDE calibration, the MIP energy-deposition model, and cell-to-cell light-collection variations. Their quantitative evaluation is the subject of ongoing characterisation. The p.e./MIP ratio is obtained directly from the most probable value of the Landau fit to the SiPM charge spectrum expressed in photoelectrons. Dividing by the unit MIP energy deposit yields the photoelectron-to-MIP conversion. This value is adopted as the experimental MIP reference for the active unit. The S13360-3050PE device used for this fiducial measurement has a weighted PDE of 32.5% for the GFO emission spectrum. This provides a cross-calibrated MIP reference, which is adopted as the empirical light-output scale for the simulation.

The third measurement used 5 GeV electrons at the KEK test beam, read out with an NDL EQR20-11-3030 SiPM. The Landau-fitted MPV is 157.6 ± 2.9 p.e./MIP (Fig. 5(c)). The

higher signal relative to the cosmic-ray result is expected. A 5 GeV electron initiates an electromagnetic shower within the dense GFO glass rather than depositing energy as a single minimum-ionising track. The p.e./MIP unit is retained here solely as a normalisation convenience. The electron measurement demonstrates that the cell can sustain shower-level energy deposits without saturation, which is relevant for the calibration and dynamic-range requirements of the full detector readout chain.

The three independent measurements together confirm that the single-cell SiPM signal is well above the single-photoelectron noise floor. This provides adequate margin for the 0.1 MIP readout threshold described in Section II C. The results meet the requirement for prototype beam-test operation and define the input scale for the detector-level digitisation model (Section IV).

The cosmic-ray result merits particular attention in relation to the optical simulation. The Geant4 model described in Section II C uses the methodology of Ref. [12] with GFO-specific optical parameters. It predicts a response of about 42 p.e./MIP for a $40 \times 40 \times 10$ mm^3 cell with Teflon wrapping and a 3×3 mm^2 SiPM. The measured cosmic-ray value of 63.6 ± 0.5 p.e./MIP exceeds this prediction by roughly 50%. The discrepancy is attributed to simplifications in the optical model, including the description of light collection and of the SiPM response. The cosmic-ray measurement employed a sensor with a weighted PDE of 32.5% [2]. A numerical decomposition of the discrepancy has not yet been performed, and the associated simulation uncertainty remains at the 50 % level. A GFO-specific optical calibration, informed by the present cell measurements, is therefore a priority for the prototype programme.

In a first production batch of approximately 290 $40 \times 40 \times 10$ mm^3 tiles, $60 \pm 3\%$ (stat) met the 1000 ph/MeV PMT-based light-yield target. This figure applies to the first 290-tile production batch, whereas the laboratory result demonstrates the material's potential. Systematic uncertainties associated with the testing procedure have not yet been evaluated. Tile-to-tile variation is under active investigation and is expected to be reduced through improved melting, casting, and annealing procedures. Production uniformity is a central concern for detector-scale deployment of glass scintillator. The concept includes tile-level quality control before installation, together with in-situ MIP and LED monitoring after detector operation begins (Section V A). The present yield, while not yet at the level required for mass production, demonstrates that tiles meeting the specification can be produced in reasonable quantity. The characterisation infrastructure required for batch testing is being established in parallel with the material development programme.

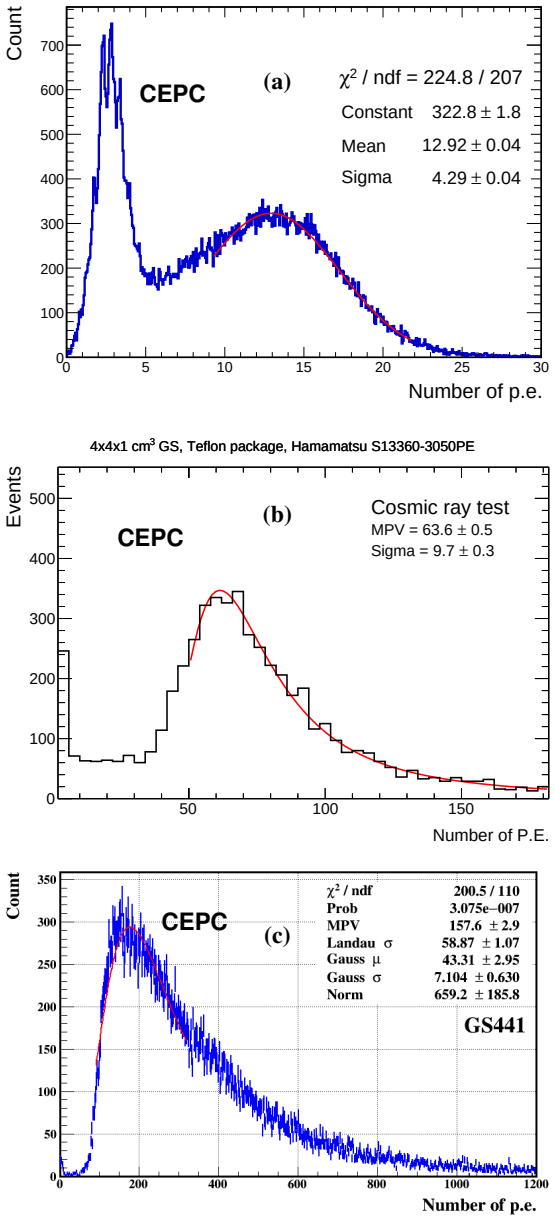

Fig. 5: Single-cell photoelectron responses measured with three complementary probes: (a) ^{137}Cs pulse-height spectrum (HPK S14160-3050HS), MPV = 12.9 p.e. at 662 keV; (b) cosmic-ray muon response (HPK S13360-3050PE), 63.6 ± 0.5 p.e./MIP; (c) 5 GeV electron beam at KEK (NDL EQR20-11-3030), Landau MPV 157.6 ± 2.9 p.e./MIP. All measurements used Teflon wrapping and a centrally coupled SiPM. The SiPM models differ because the data were taken at different times as device availability evolved; all are representative of the reference specifications in Table 3.

IV. SIMULATION AND PERFORMANCE PROJECTION

The measured cell properties reported in the preceding section—light output, attenuation length, and signal amplitudes—provide the input parameters for the detector-level digitisation simulation described below.

A. Simulation setup and single-hadron response

The intrinsic response of the GS-HCAL is evaluated with Geant4 in the CEPCSW framework [1]. This evaluation uses a standalone HCAL configuration and a digitisation model that incorporates the best available experimental inputs. Birks' quenching [23] is modelled with $k_B = 0.01$ cm/MeV, the standard value for organic plastic scintillator. This value is adopted here as a preliminary placeholder pending a dedicated measurement for inorganic GFO glass. The applicability of the Birks formalism to inorganic glass scintillators has not been experimentally verified. The effective light output is set to 60 p.e./MIP, empirically calibrated from the cosmic-ray measurement of 63.6 ± 0.5 p.e./MIP (Section III) with a conservative downward adjustment to account for tile-to-tile variation. This value is anchored to the single-cell cosmic-ray measurement of 63.6 ± 0.5 p.e./MIP (Section III). The exact p.e./MIP distribution from QC-passing tiles has not yet been measured. The 5.7 % margin is expected to bracket the variation observed in the first 290-tile production run. A direct p.e./MIP uniformity campaign is planned as part of the prototype tile qualification. The attenuation length measured on the best-performing laboratory sample is 6 cm (Section III A). The distribution among production tiles has not yet been characterised. The simulation therefore uses this best value as a placeholder, and a dedicated attenuation-length uniformity study is planned for the prototype programme. A 0.1 MIP readout threshold is applied as a baseline digitisation parameter. These digitisation parameters are preliminary and await validation with full prototype beam-test data. They form the present working basis for performance projection.

The single-hadron energy resolution is parametrised in the standard form $\sigma_E/E = a/\sqrt{E} \oplus b$, where a is the stochastic term and b the constant term. With the present digitisation model, the projected standalone GS-HCAL response is $29.8\%/\sqrt{E\,[\mathrm{GeV}]} \oplus 6.5\%$, with energy non-linearity within 2% over the range from a few GeV to several hundred GeV. The stochastic and constant terms are obtained from a fit to simulated energy points. The fit uncertainties are not yet quoted and will be evaluated in a dedicated study with larger simulation statistics. The resolution and linearity results are shown in Fig. 6.

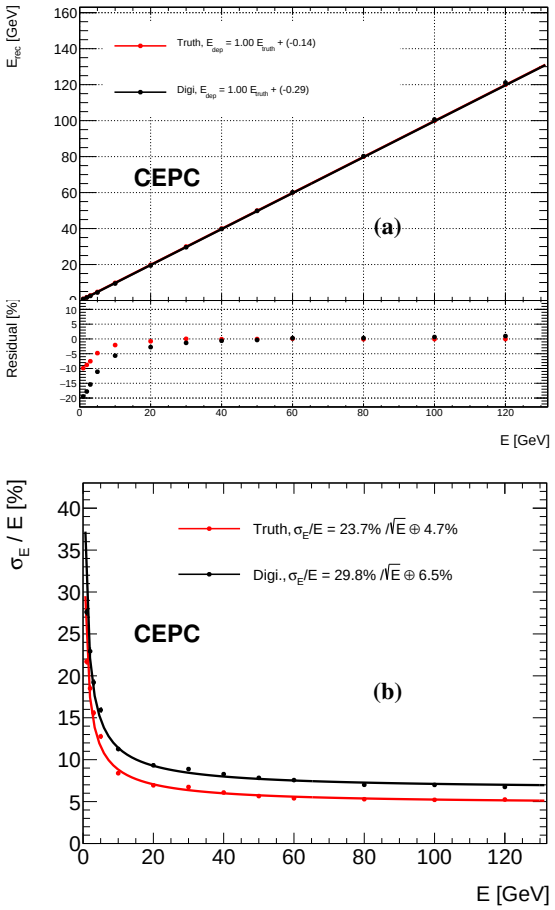

Fig. 6: Projected standalone GS-HCAL single-hadron response from the full digitisation-based Geant4 simulation: (a) energy linearity—reconstructed versus true energy for single hadrons in the standalone GS-HCAL, non-linearity within 2% over the full energy range; (b) energy resolution as a function of incident hadron energy, with fitted parametrisation $29.8\%/\sqrt{E} \oplus 6.5\%$.

B. Constant term decomposition

The total constant term of 6.5% includes contributions from longitudinal shower leakage, digitisation effects, and intrinsic response non-uniformities. Parameter scans indicate that a MIP-scale signal above 60 p.e./MIP is important for stable operation at a 0.1 MIP threshold. The measured attenuation length of 6 cm provides adequate uniformity. A dedicated Geant4 scan of k_B (shown in the CEPC Reference TDR [2]) demonstrates the hadronic resolution sensitivity to the Birks constant. The systematic shift on the constant term and its propagation to the boson mass resolution have not yet been quantified. They will be evaluated once a GFO-specific quenching measurement is available.

To isolate the leakage contribution, a dedicated depth-variation study was performed in which the simulated HCAL thickness is increased from $6\,\lambda_\mathrm{I}$ to $10\,\lambda_\mathrm{I}$ while all digitisation parameters are held fixed. The constant term attributable to longitudinal leakage alone is $b_\mathrm{leakage} \approx 4.7\%$ at $6\,\lambda_\mathrm{I}$, reducing to about 2.9% at $10\,\lambda_\mathrm{I}$. Decomposing the total constant term in quadrature, $b^2_\mathrm{total} = b^2_\mathrm{leakage} + b^2_\mathrm{other}$, yields $b_\mathrm{other} = \sqrt{(6.5\%)^2 - (4.7\%)^2} \approx 4.5\%$. This residual is attributed to digitisation effects including the 0.1 MIP threshold, the 6 cm attenuation length, Birks quenching, and intrinsic response non-uniformities. The quadrature subtraction assumes that the leakage contribution is uncorrelated with the other effects. The sub-decomposition of b_other therefore represents a model-dependent attribution that will be experimentally disentangled through prototype beam-test characterisation. At $10\,\lambda_\mathrm{I}$, where $b_\mathrm{leakage} \approx 2.9\%$, the projected total constant term becomes $\sqrt{(2.9\%)^2 + (4.5\%)^2} \approx 5.4\%$. Software compensation techniques of the kind demonstrated on

the CALICE AHCAL [21] are expected to further reduce the effective leakage contribution [15]. Their quantitative impact on the GS-HCAL has not yet been evaluated.

C. Electron–hadron response and $H \to gg$ benchmark

The calibration constant C relates the raw HCAL signal S_{HCAL} to the true particle energy through $E_{\mathrm{true}} = C \cdot S_{\mathrm{HCAL}}$. The ratio C_{hadron}/C_e characterises the electron–hadron response balance of the calorimeter. The simulated values are summarised in Table 4, and range from 1.09 ± 0.02 for π^- to 1.14 ± 0.02 for protons and neutrons. They indicate a smaller signal for hadrons than for electrons at the same energy. This behaviour is typical of a non-compensating sampling calorimeter. The high density of the GFO active medium and the Birks quenching correction affect the relationship between the calibration constant C and the intrinsic e/h ratio [20]. The intrinsic e/h response ratio remains to be extracted through decomposition of electromagnetic and hadronic shower components.

TABLE 4: Calibration constants C and electron–hadron response ratios C_{hadron}/C_e for the GS-HCAL.

Particle	C	C_{hadron}/C_e
e^-	2.94 ± 0.01	—
π^-	3.20 ± 0.05	1.09 ± 0.02
K^+	3.28 ± 0.05	1.12 ± 0.02
n	3.35 ± 0.07	1.14 ± 0.02
p	3.36 ± 0.07	1.14 ± 0.02

The $H \to gg$ benchmark provides the most direct test of whether the HCAL concept, combined with PFA reconstruction, meets the CEPC physics requirements. The analysis uses WHIZARD [22] for event generation. It uses Geant4 in CEPCSW for full detector simulation with particle-flow reconstruction. The reconstructed dijet invariant mass distribution yields $m_{jj} = 126.32 \pm 0.04$ GeV/c^2 and a width of $\sigma(m_{jj}) = 4.90 \pm 0.04$ GeV/c^2. This corresponds to a boson mass resolution (BMR) of $3.88 \pm 0.03\%$ (statistical only), as shown in Fig. 7. The reconstructed mass offset of about 1.3 GeV/c^2 is relative to the nominal Higgs mass of 125 GeV. It is attributable to jet energy scale effects in the PFA reconstruction chain. It is within the expected range for dijet mass measurements at this energy. The BMR of 3.88% is consistent with the CEPC target of 3–4% for hadronic final states.

These simulation results establish the expected performance under the present modelling assumptions and motivate the next step of experimental validation with a calibrated prototype.

V. PROTOTYPE PROGRAMME AND OUTLOOK

The simulation projections presented in Section IV demonstrate that the GS-HCAL concept meets its physics performance targets under the present modelling assumptions. Realising this design at the full CEPC detector scale requires a coherent effort of engineering validation, calibration development, and prototype beam testing. The present section defines that effort and identifies the key remaining uncertainties that the prototype is designed to resolve.

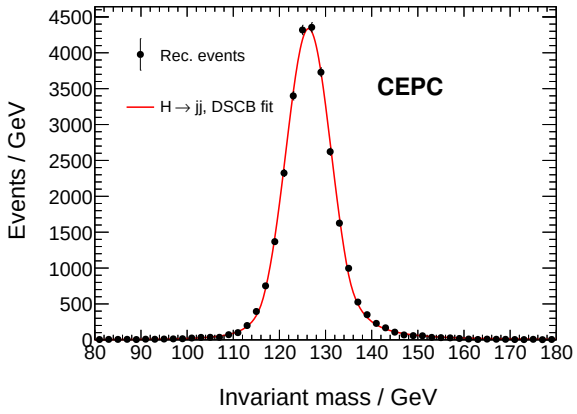

Fig. 7: Reconstructed dijet invariant mass distribution for the $H \to gg$ benchmark with particle-flow reconstruction. The fit yields $m_{jj} = 126.32 \pm 0.04$ GeV/c^2 and $\sigma = 4.90 \pm 0.04$ GeV/c^2, corresponding to a boson mass resolution of 3.88%.

A. Engineering feasibility and calibration

The GS-HCAL structure has been evaluated through finite-element analysis (FEA) to verify that it can be mechanically realised at detector scale. The present analyses address static gravitational loads and assembly stresses. Dedicated studies of dynamic loading (seismic and transport vibration) and thermal-stress arising from expansion-coefficient mismatches are planned as part of the engineering validation programme. During assembly, maximum deformations are below 0.66 mm. Under the 135 t electromagnetic calorimeter (ECAL) load, peak stresses of 371 MPa at connection points correspond to safety factors above 2.2 with titanium-alloy TC4 components. GS cell stresses of about 20 MPa are well within material limits, confirming that the active elements are not mechanically at risk. These margins provide confidence that the structure meets the stability and alignment requirements of a large-scale collider detector.

Calibration is integral to the design because of the 5.22 million channels and the measured tile-to-tile response variation reported in Section III. The strategy exploits the detector's own physics data. MIP inter-calibration using prompt muons from $Z \to \mu^+\mu^-$ decays provides about 47 events per hour per cell-size window on the central barrel surface at the nominal Z-pole luminosity. This yields per-cell MIP anchors with adequate statistics. With two weeks of dedicated Z-pole data-taking, 4.71×10^8 di-muon events can be accumulated, achieving a per-cell MIP calibration precision of about 1%. Hadronic-scale inter-calibration using $Z \to q\bar{q}$ dijet

mass constraints and E/p monitoring with isolated charged hadrons link the cell-level calibration to the jet energy scale. A light-emitting diode (LED) hardware monitoring system tracks SiPM gain and linearity stability between physics fills. Together, these elements provide a self-contained calibration chain that covers the full signal chain from photoelectron to jet energy. The calibration methods described here are enabling infrastructure, not primary performance results. Their development is a prerequisite for prototype operation and will be exercised in the beam-test campaign described below.

B. Prototype design

A full technological prototype is planned to resolve the key remaining uncertainties identified in this paper. It follows the same single-layer design of Section II B. The prototype consists of a steel-scintillator sandwich of dimensions 52.0 cm × 52.0 cm × 130 cm (129.6 cm active stack plus 4 mm end plates). It comprises 48 layers of 13 × 13 arrays of $40 \times 40 \times 10$ mm^3 cells, totalling 8112 GS cells. This corresponds to $48 \times 27.0\,\text{mm} = 129.6\,\text{cm}$ of active stack plus end plates and totalling $6\,\lambda_\text{I}$. The 52.0 cm transverse dimension was chosen as a compromise between lateral shower containment and practical construction scale. Simulation of this configuration with 80 GeV π^- beams indicates roughly 95% lateral shower containment (obtained with the QGSP_BERT physics list) and a projected single-hadron energy resolution of $45\%/\sqrt{E} \oplus 8\%$. No systematic variation of physics lists has been performed for this estimate. A model-comparison study is planned during the beam-test programme. The larger stochastic term relative to the full detector projection ($29.8\%/\sqrt{E}$, Section IV A) arises from lateral shower leakage in the smaller 52 cm footprint. The constant term of 8% reflects both this lateral leakage and the digitisation effects already characterised for the full detector. The prototype is instrumented with the same front-end readout and cooling single-layer architecture, so that the complete signal chain is exercised under realistic operating conditions.

The prototype effort targets five interconnected validation goals. First, the optical model will be tested by comparing prototype beam response with Geant4 predictions at the tile and layer level. This will address the 50% simulation–measurement discrepancy identified in Section III. Second, the Birks quenching constant for GFO glass will be determined from the measured hadron energy deposition. This will replace the provisional organic-scintillator value adopted in the present simulation. Third, the intrinsic e/h response ratio will be extracted through electromagnetic and hadronic shower decomposition using particle-identified beams. Fourth, the calibration chain—MIP inter-calibration, hadronic inter-calibration, and LED monitoring—will be exercised end to end. Fifth, the system-level hadronic response, including software-compensation techniques [21], will be measured and compared with the simulation projections of Section IV. Achieving these goals will transform the present performance projections. These projections are conditional on simulation inputs and will become experimentally anchored measurements.

C. Remaining uncertainties and priorities

The following specific, well-defined uncertainties are the target of the prototype effort. It is appropriate to identify them clearly so that the programme's objectives are understood as responsive rather than open-ended.

The most significant uncertainty concerns the optical model. The present Geant4 simulation is based on the methodology of Ref. [12]. It uses GFO-specific optical parameters taken from the measurements of Sections III A and III. The simulation predicts a cosmic-ray muon response of about 42 p.e./MIP. The measured value is 63.6 ± 0.5 p.e./MIP, as reported in Section III. This 50% discrepancy indicates that the scintillation-yield and light-collection description requires GFO-specific tuning beyond simple material-parameter substitution. A dedicated optical-model calibration campaign, informed by the prototype beam-test data, will bring simulation and measurement into agreement. It is the single most impactful near-term activity for reducing systematic uncertainties on the detector performance projections.

The second uncertainty concerns the Birks quenching constant. The present simulation uses $k_B = 0.01$ cm/MeV, the standard value for organic plastic scintillators [23], as a provisional placeholder. The applicability of the Birks formalism to inorganic glass scintillators has not been experimentally verified. The constant-term decomposition in Section IV B indicates that Birks quenching has a significant effect on hadronic resolution. A dedicated hadron-beam measurement of the GFO Birks constant is therefore an essential deliverable of the prototype programme. Similarly, the intrinsic e/h response ratio has not yet been extracted from the simulated shower decomposition. Particle-identified beam data will enable this extraction and provide an experimentally grounded comparison with the calibration-slope ratios reported in Table 4.

The third area concerns tile production. As noted in Section III B, about 290 tiles have been produced to date, with about 60% satisfying the 1000 ph/MeV light-yield quality threshold. The required uniformity and yield concern the 8112-cell prototype and ultimately the 5.22 million channels of the full detector. They require further optimisation of the glass production process, including melt homogeneity and post-production quality control. This is an engineering-scale activity that can proceed in parallel with the beam-test programme.

Finally, it must be acknowledged that the systematic uncertainties associated with the present modelling assumptions—the optical model, the Birks constant, and the simulation inputs—have not yet been quantified. The quoted single-hadron resolution of $29.8\%/\sqrt{E} \oplus 6.5\%$ and the $H \to gg$ boson mass resolution of 3.88% are therefore conditional on the present parameter set. They should be understood as performance projections, not measurements. Resolving these systematic uncertainties is precisely the purpose of the prototype

effort. Their quantification will be a principal outcome.

Within the landscape of highly granular hadron calorimetry, the GS-HCAL concept occupies a distinctive and well-motivated position. Its high-density GFO glass (6.0 g/cm^3) provides a sampling fraction of about 30%. The $H \to gg$ boson mass resolution of 3.88% with PFA reconstruction meets the CEPC physics requirement of 3–4% for hadronic final states (Section IV). This design space—high-density inorganic scintillator, SiPM readout, and PFA-compatible granularity—defines a coherent approach that is distinct from, and complementary to, the established AHCAL and SDHCAL technologies.

The immediate priorities flow directly from the uncertainties identified above. The prototype beam-test campaign is the central activity. It simultaneously addresses the optical model, the Birks constant, and the intrinsic e/h extraction. In parallel, optical-model tuning using the prototype data will close the simulation–measurement gap. Software-compensation development will translate the raw hadronic response into the calibrated jet energy scale. Tile-production optimisation will demonstrate the scalability of the GFO glass technology. These activities are defined, resourced, and sequenced. Together, they form a coherent plan. Its milestones are the prototype beam tests, the release of experimentally validated performance parameters, and the demonstration that GS-HCAL technology can be manufactured at CEPC detector scale.

VI. CONCLUSION

This paper has assembled the experimental and simulation evidence that supports the GS-HCAL as the hadronic calorimeter of the CEPC reference detector. The full-scale architecture has been specified. The properties of the GFO active material have been characterised with multiple probes. The projected performance has been evaluated using a digitisation-based simulation framework.

The measurements confirm that GFO glass provides the needed combination of density, light yield, attenuation length, and radiation tolerance. The single-hadron and boson-mass resolution projections demonstrate that the design is consistent with the CEPC physics goals under the present modelling assumptions. The boson-mass resolution of 3.88 % has been evaluated only for the $H \to gg$ channel. Benchmarks for $Z \to q\bar{q}$ and $W \to q\bar{q}$ have not yet been simulated. Moreover, this projection depends on provisional values for the Birks quenching constant (taken from organic scintillator) and the optical model, whose systematic uncertainties have not been quantified. At the same time, several open questions remain. The optical simulation currently underestimates the measured single-cell response by about 50%. The Birks quenching constant for GFO has not yet been measured, and the intrinsic e/h ratio has yet to be extracted from data. Quantifying the associated systematic uncertainties is a prerequisite for turning the present performance projections into definitive results.

The prototype beam-test programme is the critical next milestone. It will validate the Geant4 optical model with GFO-specific data and determine the Birks quenching constant and intrinsic e/h ratio. It will exercise the full calibration chain from MIP inter-calibration to hadronic mass calibration. It will also measure the system-level hadronic response in a controlled beam environment. These measurements will transform the current simulation-based performance projections into experimentally validated results. They will also complete the technical basis of the GS-HCAL.

ACKNOWLEDGEMENTS

The authors thank the CEPC Study Group, the CALICE Collaboration, and the staff of the KEK test-beam and APEP proton-irradiation facilities.

[1] CEPC Study Group, CEPC Conceptual Design Report: Volume 2 – Physics & Detector, arXiv:1811.10545 (2018). doi: 10.48550/arXiv.1811.10545

[2] CEPC Study Group, CEPC Reference Detector Technical Design Report, arXiv:2510.05260 (2025). doi: 10.48550/arXiv.2510.05260

[3] M.A. Thomson, Particle Flow Calorimetry and the PandoraPFA Algorithm, Nucl. Instrum. Meth. A **611**, 25–40 (2009). doi: 10.1016/j.nima.2009.09.009

[4] M. Ruan, H. Videau, Arbor, a new approach of the Particle Flow Algorithm, in *Proceedings of the International Conference on Calorimetry for the High Energy Frontier*, pp. 316–324 (2013). doi: 10.48550/arXiv.1403.4784

[5] U. Buchner, J.P. Donker, B. Spaan, *et al.*, Performance of a scintillating glass calorimeter for electromagnetic showers, Nucl. Instrum. Meth. A **272**, 695 (1988). doi: 10.1016/0168-9002(88)90750-4

[6] Z.H. Hua, W.C. Li, S. Qian, *et al.*, Scattering model of Ce^{3+}-doped high gadolinium fluoro-oxide glass in scintillation progress, Ceram. Int. **51**, 23367–23373 (2025). doi: 10.1016/j.ceramint.2025.03.025

[7] Z.H. Hua, *et al.*, R&D of glass scintillator for nuclear radiation detection, JINST **18**, C12003 (2023). doi: 10.1088/1748-0221/18/12/C12003

[8] Z.H. Hua, *et al.*, An evaluation method for nuclear radiation detection performance of glass scintillator, Radiat. Detect. Technol. Methods **8**, 1107–1119 (2024). doi: 10.1007/s41605-024-00453-0

[9] A. Phunpueok, *et al.*, Comparison of scintillation light yield of CWO and BGO single crystals for gamma ray detection, Appl. Mech. Mater. **901**, 89–94 (2019).

[10] V. Dormenev, *et al.*, Multipurpose Ce-doped Ba-Gd silica glass scintillator for radiation measurements, Nucl. Instrum. Meth. A **1015**, 165762 (2021). doi: 10.1016/j.nima.2021.165762

[11] C. Adloff, *et al.* (CALICE Collaboration), Construction and commissioning of the CALICE analog hadron calorimeter prototype, JINST **5**, P05004 (2010). doi: 10.1088/1748-0221/5/05/P05004

[12] G. Tang, *et al.*, Optical and scintillation properties of aluminoborosilicate glass, Opt. Mater. **130**, 112585 (2022). doi: 10.1016/j.optmat.2022.112585

[13] S. Agostinelli, *et al.* (GEANT4 Collaboration), Geant4—a simulation toolkit, Nucl. Instrum. Meth. A **506**, 250–303 (2003). doi: 10.1016/S0168-9002(03)01368-8

[14] X.Y. Wang, H.Y. Zhang, D.Q. Fang, *et al.*, Design and performance of a high-speed and low-noise preamplifier for SiPM, Nucl. Sci. Tech. **34**, 11 (2023). doi: 10.1007/s41365-023-01328-7

[15] J.B. Liu, Y. Liu, W. Ootani, *et al.*, CALICE scintillator-SiPM calorimeter prototypes: R&D highlights and beamtests, Nucl. Instrum. Meth. A **1072**, 170191 (2025). doi: 10.1016/j.nima.2024.170191

[16] M. Janecek, Reflectivity spectra for commonly used reflectors, IEEE Trans. Nucl. Sci. **59**, 490–497 (2012). doi: 10.1109/TNS.2012.2183385

[17] Y.Y. Liu, H.T. Jing, L.S. Huang, *et al.*, Physical design of the APEP beam line at CSNS, Nucl. Instrum. Meth. A **1042**, 167431 (2022). doi: 10.1016/j.nima.2022.167431

[18] S.H. Yin, P. Hu, S. Qian, *et al.*, Radiation resistance study of Gd-Al-B-Si-Ce^{3+} glass scintillators using 80 MeV proton beam irradiation, Nucl. Instrum. Meth. A **1081**, 170869 (2026). doi: 10.1016/j.nima.2025.170869

[19] P. Hu, S. Qian, H. Cai, *et al.*, Radiation resistance study of the Gadolinium Fluoro-Oxide glass scintillator under gamma-ray irradiation, Nucl. Instrum. Meth. A **1088**, 171529 (2026). doi: 10.1016/j.nima.2026.171529

[20] N. Akchurin, R. Wigmans, Hadron calorimetry, Nucl. Instrum. Meth. A **666**, 80–97 (2012). doi: 10.1016/j.nima.2011.10.035

[21] S. Lai, *et al.* (CALICE Collaboration), Software compensation for highly granular calorimeters using machine learning, JINST **19**, P04037 (2024). doi: 10.1088/1748-0221/19/04/P04037

[22] W. Kilian, T. Ohl, J. Reuter, WHIZARD: Simulating multi-particle processes at LHC and ILC, Eur. Phys. J. C **71**, 1742 (2011). doi: 10.1140/epjc/s10052-011-1742-y

[23] J.B. Birks, Scintillations from organic crystals: Specific fluorescence and relative response to different radiations, Proc. Phys. Soc. A **64**, 874–877 (1951). doi: 10.1088/0370-1298/64/10/303

[24] R.Y. Zhu, D.A. Ma, H.B. Newman, *et al.*, A study on the properties of lead tungstate crystals, Nucl. Instrum. Meth. A **376**, 319–334 (1996). doi: 10.1016/0168-9002(96)00286-0